American Mineralogist, Volume 83, pages 553–568, 1998

Quantitative arsenic speciation in mine tailings using X-ray absorption spectroscopy

Andrea L. Foster,[1,*] Gordon E. Brown Jr.,[1,2] Tracy N. Tingle,[1,3†] and George A. Parks[1]

[1]Department of Geological and Environmental Sciences, Stanford University, Stanford, California 94305-2115, U.S.A.
[2]Stanford Synchrotron Radiation Laboratory, Stanford, California 94309, U.S.A.
[3]Center for Materials Research, Stanford University, Stanford, California 94305-4045, U.S.A.

Abstract

X-ray absorption fine structure spectroscopy (XAFS) was used to determine arsenic (As) oxidation state, local coordination (to a radius of ≈7 Å around As), and the relative proportion of different As species in model compounds and three California mine wastes: fully oxidized tailings (Ruth Mine), partially oxidized tailings (Argonaut Mine), and roasted sulfide ore (Spenceville Mine). Mineralogy was characterized by Rietveld refinement of X-ray powder diffraction patterns. The spatial distribution of As in the mine wastes (at several micrometers spatial resolution) was determined by electron microprobe analyses. X-ray absorption near edge structure (XANES) analysis indicates that As^{5+} is the dominant oxidation state in the mine samples, but mixed oxidation states (nominally As^0 and As^{5+}) were observed in the Argonaut Mine waste. Non-linear, least-squares fits of mine waste EXAFS (Extended XAFS) spectra indicate variable As speciation in each of the three mine wastes: As^{5+} in the Ruth Mine sample is sorbed on ferric oxyhydroxides and aluminosilicates (probably clay) in roughly equal portions. Tailings from the Argonaut Mine contain ≈20% As bound in arsenopyrite (FeAsS) and arsenical pyrite ($FeS_{2-x}Asx$) and ≈80% As^{5+} in a precipitate such as scorodite ($FeAsO_4 \cdot 2H_2O$); however, no precipitate was detected by X-ray diffraction or microprobe analysis, suggesting that the phase is poorly crystalline or has low abundance (total As in sample = 262 ppm). Roasted sulfide ore of the Spenceville Mine contains As^{5+} substituted for sulfate in jarosite [$KFe_3(SO_4)_2(OH)_6$] or incorporated in the structure of an unidentified Ca- or K-bearing phase, and As^{5+} sorbed to the surfaces of hematite or ferric oxyhydroxide grains. Determination of solid-phase As speciation in mine wastes by XAFS spectroscopy is a valuable first step in the evaluation of its bioavailability, because the mobility and toxicity of As compounds vary with oxidation state. As bound in precipitates, as in the Argonaut mine sample, is considered to be less available for uptake by organisms than when sorbed on mineral surfaces or coprecipitated with poorly crystalline phases, as found for the Ruth and Spenceville mine wastes.

Introduction

Arsenic (As) is a common constituent of sulfide deposits, often present at the 2–3 wt% level in copper and lead ores and as high as 11 wt% in gold ores (Cullen and Reimer 1989; Azcue and Nriagu 1994). Chronic As poisoning in humans has been associated with the use of contaminated well water from As-bearing aquifer material (Cebrian 1994; Chen 1994; Singh 1995). In arid mining regions or near active smelters, an additional pathway for As exposure exists by ingestion or inhalation of As-rich particulates (Cebrian 1994). Inadvertent or inappropriate use of mine tailings, coal fly ash, and other As-rich surficial material poses a potential threat to human health (e.g., Greenwald 1995; Vogel 1995).

A realistic evaluation of the risk posed by As-bearing tailings piles depends on accurate determination of As speciation, because its toxicity and mobility varies with oxidation state and chemical environment. For example, in vivo studies indicate that the toxicity of reduced As compounds such as gallium arsenide [and by analogy, elemental arsenic (As^0) and arsenopyrite (FeAsS)] are significantly lower than inorganic As compounds containing As^{3+} and As^{5+}, mainly because of their lower solubility (Yamauchi and Fowler 1994). However, upon ingestion reduced arsenic compounds are slowly converted to inorganic As^{3+} and or As^{5+} (Cullen and Reimer 1989). Both As^{3+} and As^{5+} form anionic species when in aqueous solution, adsorbed to mineral surfaces, or incorporated into precipitates. As^{5+} adsorbs more strongly to mineral surfaces than does As^{3+}, thus is generally less mobile (Frost and Griffin 1977; Korte and Fernando 1991).

The mobility of As released during the microbially mediated weathering of sulfide ore and pyrite-bearing shales is

* E-mail: andrea@pangea.stanford.edu.
† Deceased.

0003–004X/98/0506–0553$05.00

subject to both solubility and adsorption controls. For example, As in As_2S_3 (orpiment), FeAsS (arsenopyrite), and Cu_3AsS_4 (enargite) can be oxidized to a mixture of As^{3+} and As^{5+} by monocultures of *T. ferrooxidans*, with the concomitant formation of scorodite ($FeAsO_4 \cdot 2H_2O$) or jarosite [$KFe_3(SO_4)_2(OH)_6$; Erlich 1995]. Arsenic oxyanions readily sorb to ferric hydroxide phases, which are often present as colloidal precipitates in drainage waters and as surface-bound precipitates on mineral grains (Pierce and Moore 1982; Waychunas et al. 1993, 1995; Manceau 1995). Clay minerals are also a potential sink for oxidized As species, particularly in shales and soils (Anderson et al. 1975; Goldberg and Glaubig 1988; Spackman et al. 1990). In As-rich mine tailings piles, precipitates such as scorodite, $Fe_2(AsO_4)_3 \cdot 8H_2O$ (parasymplesite), or $Ca_3(AsO_4)_2 \cdot 10H_2O$ (rauenthalite) may form, often as surface coatings on other mineral grains (Rimstidt et al. 1994; Erlich 1995). Alternatively, As oxyanions can substitute in common secondary minerals including jarosite, $CaSO_4 \cdot 2H_2O$ (gypsum), $CaCO_3$ (calcite), and $Ca_6Al_2(SO_4)_3(OH)_{12} \cdot 26H_2O$ (ettringite; Tanji et al. 1992; Myneni et al. 1997).

One of the difficulties encountered in evaluating the potential health risks of As in mine tailings is accurate determination of its speciation in different solid phases and its possible presence as a surface-bound or adsorbed species (which if present could represent a more mobile form relative to As bound in solid phases). Selective chemical extraction is often used to determine the amounts of surface-bound As, but it does not provide much information about As species in relatively insoluble precipitates or as coatings on mineral particles or in fine-grained primary minerals or smelter products. X-ray absorption fine structure spectroscopy (XAFS), in combination with methods such as quantitative phase analysis of X-ray diffraction patterns, electron microprobe analyses, or scanning and transmission electron microscopy, provides a more direct means of assessing the types of As species (both surface-bound and present in crystalline or amorphous solid phases).

We have employed XAFS spectroscopy and several complementary methods to investigate the speciation of As in six well-characterized model compounds and three mine wastes from California gold districts: (1) highly oxidized tailings from the Ruth Mine (RM), (2) tailings with 2% residual sulfides from the Argonaut mine (AM), and (3) roasted sulfide cinders from the Spenceville mine (SM). Although XAFS spectroscopy is routinely employed for the analysis of adsorption phenomena in well-characterized synthetic samples, (e.g., Brown et al. 1989; Manceau et al. 1992; Waychunas et al. 1993; O'Day et al. 1994a; Fendorf et al. 1994a; Brown et al. 1995; O'Day et al. 1996), it has been only recently employed to determine heavy metal speciation in natural samples (e.g., Fendorf et al. 1994b; Pickering et al. 1995; Manceau et al. 1996; Peterson et al. 1997).

Materials and methods

Mine waste samples and model compounds

Sample RM consists of tailings collected from a surface impoundment at the Ruth Mine, an inactive gold mine near Trona, California. Sample RM was homogenized, dried at 105 °C for 24 h, and sieved to 325 mesh (<45 μM) prior to analysis; it contains 3650 ppm As (R.S. Borch and L.L. Hastings, unpublished data). Sample AM consists of fine-grained tailings from the Argonaut Mine near Jackson, California, contains 260 ppm As (R.S. Borch and L.L. Hastings, unpublished data) and was analyzed as collected. Sample SM from the Spenceville Mine, a copper-bearing sulfide deposit in the Smartville Mining District, east of Marysville, California, contains 51 ppm As and was analyzed without pretreatment.

Samples RM and AM were studied previously by Borch et al. (1994a, 1994b) using a four-step selective chemical extraction procedure developed by Tessier et al. (1979). Each sample was successively reacted with 0.25 M KCl, 0.1 M K_2HPO_4, 1 M NaOAc, and citrate-dithionite solutions, in that order. The extraction data for sample RM suggest that ≈2% of the As is present as easily extractable sorbed species, ≈1% is associated with carbonates, ≈6% is bound in silicates and other ''insoluble'' phases, and the remainder is sequestered in poorly crystalline ferric hydroxide phases. A similar analysis of sample AM suggests that ≈6% of the total As is easily removed, ≈2% is associated with carbonates, and only ≈2% is associated with ferric hydroxides. Borch et al. (1994b) suggest that the remaining As is present in low-solubility phases.

Synthetic samples of As^{5+} sorbed to goethite (α-FeOOH) and gibbsite [γ-$Al(OH)_3$] were prepared to serve as models of As^{5+} bound to soil minerals. High surface area solids were added to 85 mL polycarbonate centrifuge tubes and equilibrated with 0.1 M $NaNO_3$ (Baker) solutions at pH 8 for 24 h with constant end-over-end rotation. The goethite was prepared by C. Fuller (USGS, Menlo Park, California) and the gibbsite was obtained from Alcoa Corporation. The slurries were spiked with As^{5+} from 250 mM stock solutions (prepared by dissolution of solid $Na_2HAsO_4 \cdot 7H_2O$ in purified water) at pH 8. The spiked slurry was then titrated to a final pH of ≈4.0 by the dropwise addition of 0.1 M HNO_3. Spiked slurries were equilibrated for 24 h, then centrifuged at 18 000 rpm for 30 min. The supernatants were immediately decanted, and the remaining wet pastes (containing about 5% of the supernatants) were loaded into Teflon-holders with mylar windows and kept moist prior to XAFS data collection (no longer than 48 h; see below).

Native arsenic (As^0), arsenopyrite (FeAsS), and orpiment (As_2S_3) were obtained from the Stanford University mineral collection (Table 1). Scorodite ($FeAsO_4 \cdot 2H_2O$) was provided by D. Voigt of Pennsylvania State University. Reagent grade disodium orthoarsenate heptahydrate ($Na_2HAsO_4 \cdot 7H_2O$) and sodium arsenite tetrahydrate ($NaAsO_2 \cdot 4H_2O$) were utilized as crystalline model compounds.

X-ray diffraction and electron microprobe analyses

Samples were hand-ground in a silicon carbide mortar and pestle and mounted on glass microscope slides for

TABLE 1. General description of model compounds

Model Compound	Locality	Minor Phases*	Structure Report
As^0	Saxony, Germany Stanford Coll. 4283	Stibarsen (SbAs)	Schiferl and Barrett (1969)
FeAsS	Saxony, Germany Stanford Coll. 4554	Galena (PbS) Sphalerite (ZnS)	Fuess et al. (1987)
As_2S_3	Saxony, Germany Stanford Coll. 20 092	—	Mullen and Nowacki (1972)
$NaAsO_2 \cdot 4H_2O$	Aldrich	—	Sheldrick et al. (1987)
$Na_2HAsO_4 \cdot 7H_2O$	Sigma	—	Baur et al. 1970
$FeAsO_4 \cdot 2H_2O$†	Durango, Mexico	Carminite $(PbFe)_2(AsO_4)_2(OH)_2$	Hawthorne (1976)

* Determined by energy-dispersive analysis on the electron microprobe (see text).
† Scorodite provided by Don E. Voigt, Dept. of Geosciences, Pennsylvania State University.

X-ray diffraction (XRD) analysis. XRD patterns were collected over 2 to 95 °2θ with a Rigaku Geigerflex diffractometer (graphite-monochromatized Cu$K\alpha$ radiation, 0.05 °2θ steps, 3 s count time per step). The relative proportion of crystalline phases present in the mine samples was determined by Rietveld simulation of experimental XRD patterns using the program DBWS 9600PC, (Reynolds 1993; for a summary of the technique and its limitations as applied to multiphase mixtures, see Bish and Post 1993, and references therein). Starting unit-cell parameters and atomic coordinates were taken from published high-quality structure refinements when available. Global isotropic temperature factors for each phase were assigned a constant value, as in previous studies (Bish and Howard 1988). Minor phases as low as 0.2 relative wt% have been detected by Rietveld analysis using data collected under conditions similar to ours (Bish and Post 1993). The accuracy of Rietveld phase analysis can be 2.5 wt% (absolute) from studies of model mixtures, but is reduced through microabsorption of the beam by Fe-rich phases in the sample (see Bish and Post 1993). No internal standard was used in our analysis, therefore only the relative proportions of the phases considered are reported (Bish and Howard 1988).

To minimize the number of floating parameters in Rietveld calculations, the instrumental background was fit by a constant or a linear function, varying specimen displacement but not the transparency or zero point (as the latter two parameters are strongly correlated to specimen displacement and have similar effects on the calculated pattern). Phase-specific Pseudo-Voigt peak profile and peak mixing parameters were varied but constrained to either constant or linear functions. Phase-specific unit-cell parameters and preferred orientation corrections (March-Dollase function) were varied only for muscovite, which was assigned an interstitial K occupancy of 0.75 (Moore and Reynolds 1989) and used as a surrogate for illite in fits to the experimental XRD patterns of samples RM and AM. The combined effects of several parameters, including the reduced number of varied parameters, the imperfection of muscovite as a structural model for illite, and microabsorption probably degrade our accuracy somewhat more than 2.5% (Bish 1993; Bish and Post 1993).

Electron microprobe analysis (EMPA) were performed using a JEOL 733 microprobe. Samples were prepared by mounting fresh grain chips or powders in Petropoxy. Operating conditions for quantitative compositional analyses were 20 kV accelerating voltage and 15 nA beam current, with a nominal beam diameter of 2 μm; ≤ 2 μm pyrite grains in the AM tailings were analyzed at 10 keV using a 10 nA beam current (nominal beam diameter was 1 μm). Appropriate standards were collected before analyses, and standard ZAF corrections were applied to the sample data. Minor phases were identified by qualitative compositional data obtained by energy-dispersive spectrometry (EDS).

X-ray absorption fine structure (XAFS) spectroscopic analyses

Model compounds were ground to fine-grained powders using a silicon carbide mortar and pestle. Grinding was minimal for mine-waste samples. Model compounds were diluted with reagent-grade boron nitride for XAFS data collection, then loaded into 1.5 mm thick aluminum holders. Mine waste samples were loaded into 3 mm thick Teflon cells. Teflon and aluminum sample holders were enclosed on both sides by gas-permeable mylar tape.

As K-edge XAFS spectra were collected at the Stanford Synchrotron Radiation Laboratory (SSRL) on beamlines VI-2 and IV-3 over the energy range 11 635–12 900 eV (ring conditions: 3 GeV and 50–90 mA). Beamline VI-2 was equipped with a double-crystal Si (111) monochromator and a focusing mirror after the monochromator. A silicon (220) double-crystal monochromator with 1 mm vertical slits before the monochromator was employed on beamline IV-3 for XANES data collection. On both beamlines, the monochromator was detuned between 35–50% to reject harmonics when a harmonic rejection mirror was not employed. The monochromator step size was reduced to 0.15 eV per step in the XANES region (11 845–11 895 eV) to collect high-resolution spectra. XAFS data for the mine samples and model compounds were collected at ambient T and P in fluorescence and transmission modes, with the simultaneous collection of an As reference foil for energy calibration.

Our analysis of XAFS data is similar to recent procedures (O'Day et al. 1994a, 1994b, 1996; Bargar et al. 1996; Thompson et al. 1997). Data analysis was accom-

plished using the EXAFSPAK programs (George 1993a). XANES spectra of model compounds and samples were background subtracted and normalized to the edge jump (the spectral amplitude measured at 11 885 eV). The second derivative of each XANES spectrum was then calculated using a 2 eV smoothing interval. Our XANES analysis consisted of fitting linear combinations of model spectra to sample spectra using the program DATFIT (George 1993b). The precision of this fit procedure was determined to be ≈10% based on analyses of control mixtures of model compounds.

To extract information about the identity, number, and radial distance of atoms in first, second, and third shells around a central As atom, the experimental EXAFS spectrum [$\chi(k)$] is considered as the sum of photoelectron waves scattered from these shells of neighboring atoms (Stern 1974; O'Day et al. 1994a, 1994b). Ideally, the frequency of each photoelectron wave contributing to the total EXAFS spectrum can be isolated by taking a Fourier transform (FT) of the EXAFS data. In the simplest case, each peak in the FT represents correlations between one type of absorber-backscatterer pair (e.g., As and O). However, analysis of complex heterogeneous samples may be greatly complicated by the presence of multiple types of adsorber-backscatterer pairs at similar distances. Ideally, when corrected for phase-shift effects, the position of each peak in the FT (in R space, in units of angstroms) represents the radial distance from each shell of neighboring atoms to the central As atom. In reality, FT peaks often overlap, and in the worst case, multiple shells due to different absorber-backscatterer pairs can overlap to form a single peak in the FT. In order to overcome this difficulty, each peak of the experimental FT was back-transformed (Fourier filtered) to produce an EXAFS spectrum that was also analyzed by the least-squares fitting methods described below. The Fourier transforms are not phase-shift corrected, and thus peak positions are ≈ 0.3–0.5 Å less than the true distances. However, FT peak positions derived from least-squares fits and those reported in the text are corrected for this phase shift.

Theoretical EXAFS spectra were calculated using the multiple-scattering computer code FEFF6.01, hereafter referred to as FEFF6 (Rehr et al. 1992), for model compounds and adsorption samples. Given a user-defined cluster of atoms (which we generated from crystal structure reports and molecular modeling programs), FEFF6 calculates the theoretical $\chi(k)$ for each single- and multiple-scattering path meeting a specified amplitude cutoff criterion. In most of our simulations, this cutoff was set to reject any path whose amplitude was less than 20% of the maximum, thereby retaining only significant paths in the theoretical EXAFS spectrum. The many-body amplitude reduction factor (S_0) and the mean-square disorder parameter, also called the Debye-Waller parameter (σ^2) were held at 0.85 and 0.0, respectively, for determining initial values of phase-shift and amplitude functions from the single-path data of model compounds (see below); the σ^2 values of the FEFF6-generated EXAFS functions of the model compounds were further refined on a path-by-path basis until the calculated EXAFS visually matched the observed EXAFS of the model compounds. In FEFF6-generated EXAFS spectra of unknown compounds such as As sorbed on oxides or present in jarosite, the value of σ^2 for second and higher shells was constrained to 0.007 Å^2. Total phase-shift and amplitude functions for several absorber backscatterer pairs (As-O, As-As, As-S, As-Fe, As-Al, As-Ca, As-Na) were generated from FEFF6 calculations of model compound structures for which experimental EXAFS data were also obtained (see Table 1); As-Pb and As-Zn phase shift and amplitude functions were taken from a FEFF6 calculation of the mineral tsumcorite [$Pb(Zn,Fe)_2(OH,OH_2)_2(AsO_4)_2$; Tillmanns and Gebert 1973].

The Marquardt algorithm was utilized in a non-linear, least-squares routine to fit raw and Fourier-filtered EXAFS data using phase-shift and amplitude functions generated from FEFF6 calculations. ΔE_0, the difference between the user-defined threshold energy and the experimentally determined threshold energy, was varied only in the first shell, and other shells were constrained to this value. The remaining variable parameters for each shell, N (coordination number), R (interatomic distance), and σ^2 were given reasonable starting values, then fixed or floated in the fit. When fitting model compound spectra, N was almost always fixed because its value is known. In the case of mine-waste samples, σ^2 was fixed, and N and R were floated. These limitations were imposed because N and σ^2 are strongly correlated in EXAFS fits (Sayers and Bunker 1988). When fitting Fourier-filtered EXAFS data, the total number of adjusted parameters was not allowed to exceed the number of independent data points (Lytle 1989). Values for the 95% confidence limits of the estimated standard deviation (esd) of each varied parameter were obtained from fits to raw EXAFS data.

Results

X-ray diffraction and electron microprobe analyses

XRD and EMPA analyses of the mineral specimens used as model compounds (Table 1) indicate that Sb and Bi are common elemental impurities, and that most of the model compounds contain one or more minor mineral phases (some of which are also As-bearing). Our native arsenic specimen contains 10–20 modal% stibarsen ($Sb_{0.60}As_{0.40}$). In addition, the native arsenic sample contains 4 wt% Sb, probably in solid solution. Galena (PbS) and sphalerite (ZnS) are present in the arsenopyrite ($Fe_{1.00}As_{0.98}S_{1.02}$) specimen, but these minor phases are As-free to the limits of detection. The orpiment ($As_{1.97}Sb_{0.03}S_{3.00}$) specimen is monominerallic, but contains minor Sb. We observed ≈2% carminite [$(PbFe)_2(AsO_4)_2(OH)_2$] in the matrix of our scorodite ($FeAsO_4 \cdot 2H_2O$) model compound. As discussed below, EXAFS analyses of these compounds were not sensitive to these minor mineralogical and substitutional impurities.

Rietveld refinements of mine wastes gave useful information on the relative proportion of crystalline mineral

TABLE 2. General description of mine samples and results of Rietveld analyses

Mine Sample*	Locality	Mineral Phase	Relative wt% (±2.5)
Ruth Mine (RM)	Ballarat District	Illite‡	65
3650 ppm As†	Inyo County, CA, U.S.A.	Quartz (SiO_2)	24
		Calcite ($CaCO_3$)	11
Argonaut Mine (AM)	Jackson-Plymouth District	Illite‡	64
262 ppm As†	Amador County, CA, U.S.A.	Quartz	23
		Albite ($NaSi_3AlO_8$)	9
		Calcite	2
		Pyrite (FeS_2)	1
Spenceville Mine (SM)	Smartsville District	Hematite (Fe_2O_3)	76
51 ppm As§	Yuba City, CA, U.S.A.	Barite ($BaSO_4$)	13
		Jarosite ($KFe_3(SO_4)_2(OH)_6$)	3
		Quartz	8

* See Clark (1970) for more information about the gold mining districts of California; In Borch et al. 1994a and 1994b, "RM" = "RM3", "AM" = "VAN023", and "SM" = "RB0."
† R.S. Borch and L.L. Hastings, unpublished data.
‡ General formula: $(K, H_3O)Al_2Si_3AlO_{10}(OH)_2$.
§ Determined from XRF analysis.

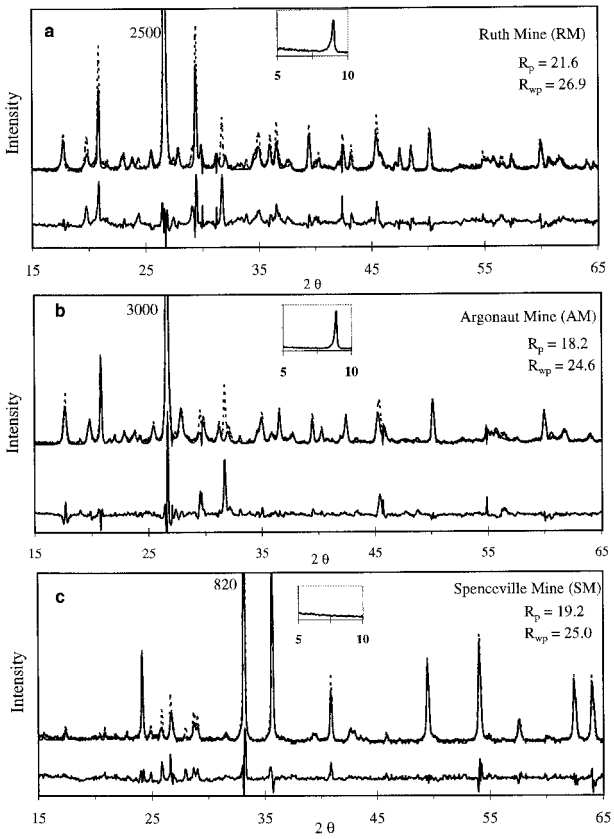

FIGURE 1. Observed (dashed line) and Rietveld-calculated (solid line) diffraction patterns of the Ruth mine (**a**), Argonaut mine (**b**), and Spenceville mine (**c**) samples. The lower curve shows the difference between observed and calculated patterns. $Rp = \Sigma|(y_{io}-y_{ic})|(\Sigma y_{io})^{-1}$ and $Rwp = [\Sigma w_i(y_{io}-y_{ic})^2(\Sigma w_i y_{io})^{-2}]^{0.5}$ where y_{io} is the observed intensity at point i, y_{ic} is the calculated intensity at point i, and w_i is a weighting parameter. See Table 2 for a summary of fit results. Patterns have been truncated in x and y to show fit details.

phases present in the mine-waste samples (Table 2). Sample RM is best fit with 65% illite, 24% quartz, and 11% calcite (Fig. 1a). EMPA maps of Fe$K\alpha$ and As$L\alpha$ X-rays demonstrate that As is mainly associated with Fe-rich material coating the major mineral phases in sample RM (Fig. 2a). The coating is inferred to be poorly crystalline ferric oxyhydroxide (e.g., ferrihydrite) because crystalline goethite was not detected by XRD.

Minor phases of high average atomic number are easily identified in sample AM using EMPA (Fig. 2b). Arsenical pyrite (0.43 wt% As) is by far the most abundant of these (≈2 modal% by image analysis), but small amounts of monazite [(Ce,La)PO_4], apatite [$Ca_5(OH,F,Cl)(PO_4)_3$], rutile (TiO_2), and sphalerite (ZnS) also exist. Arsenopyrite was observed in very small quantities (<1%). Their relative abundance determined through Rietveld calculations was always quite low (<1%), probably due to sensitivity, microabsorption, and significant peak overlap effects. Only pyrite, whose strongest line is not obscured by the peaks of more abundant phases, was included in the final Rietveld calculation, which yielded 65% illite, 22% quartz, 10% albite, 2% calcite, and 1% pyrite (Fig. 1b). Samples AM and RM both contain a prominent peak at 31.7 °2θ that was not matched by the phases considered in our analysis. This peak could be the most intense line of a second carbonate phase, but the peak does not match well with pure end-member carbonates of Ca, Mg, or Fe (although siderite gave the best fit).

Rietveld analysis indicates that the sample SM contains 76% hematite, 13% barite, 8% jarosite, and 3% quartz (Fig. 1c). EMPA-generated element maps reveal homogeneous dispersal of As in this sample (not shown).

XANES analysis

XANES spectra collected from several model compounds and adsorption samples serve as reference spectra for known oxidation states and chemical species of As (Figs. 3a and 3b). The primary feature of As K-edge XANES spectra is the absorption edge, the sharp increase in

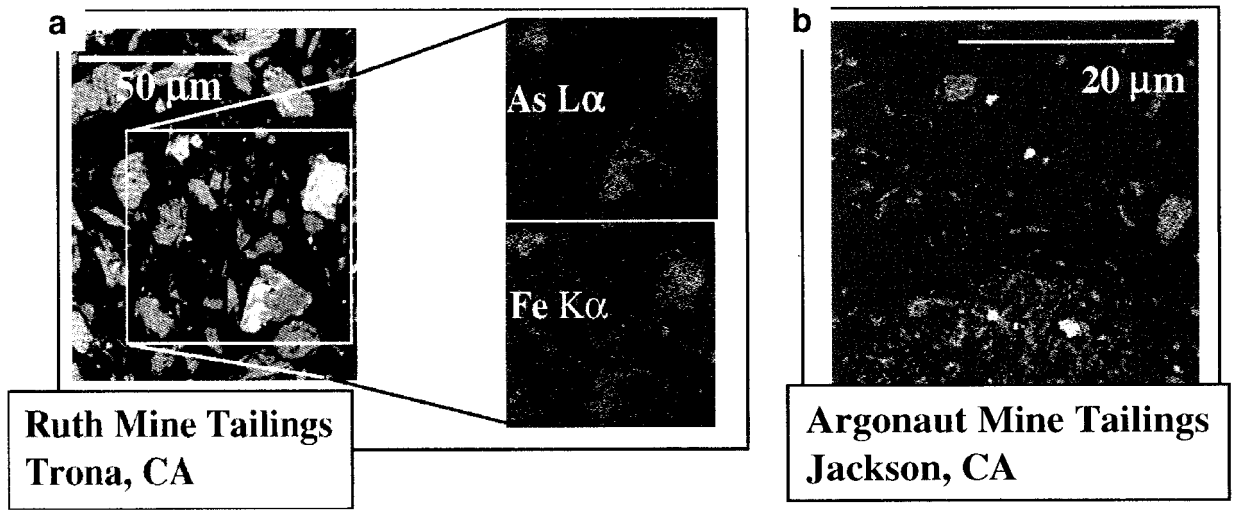

FIGURE 2. Electron microprobe images of the sample RM (**a**) showing the association of As with Fe-rich coatings on quartz and calcite grains. The leftmost figure in (**a**) is a backscattered electron (BSE) image of sample RM, in which bright areas correspond to concentrations of high-Z elements. The two images on the right are generated from element-specific wavelength scans taken over the approximate area indicated by the white box in the BSE image. The bright areas in both the As*L*α and Fe*K*α images correspond to regions of high concentration of As and Fe, respectively, and correlate well with the bright areas in the BSE. A BSE image of the VAN sample (**b**) reveals bright spots, corresponding to mineral grains of high average atomic number; the majority of these grains are pyrite.

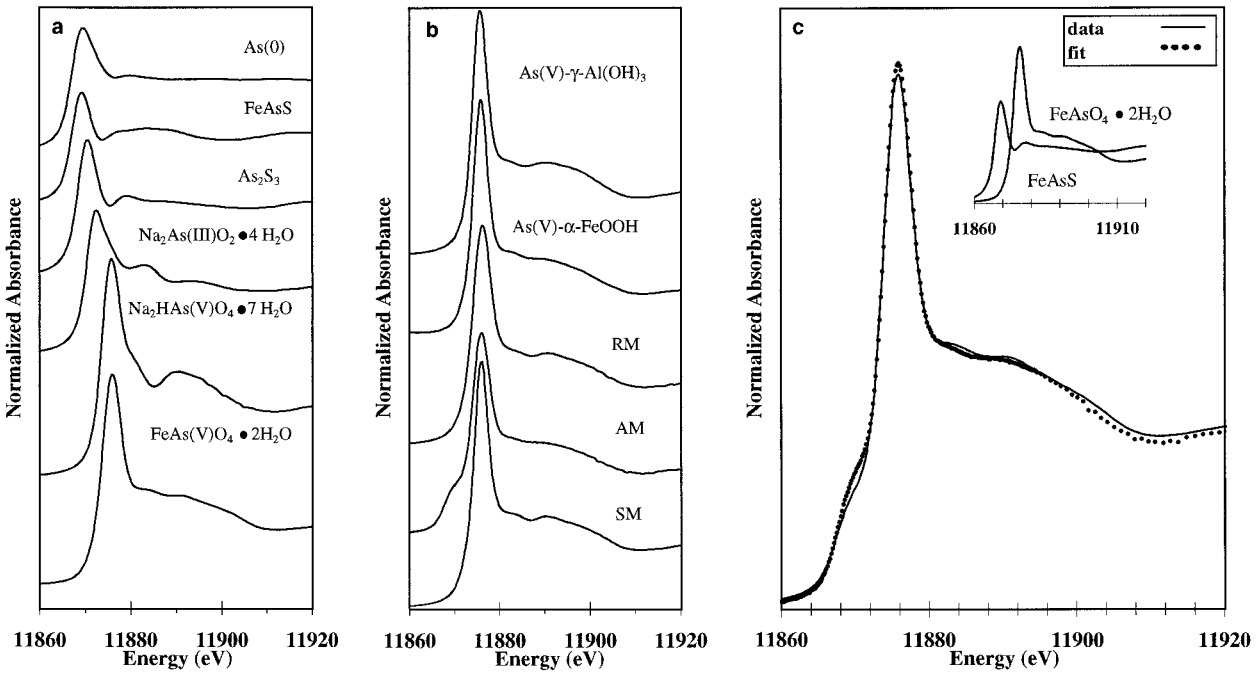

FIGURE 3. X-ray absorption near edge structure (XANES) spectra of selected model compounds (**a**) and mine-waste samples (**b**). The position of the absorption edge increases in height, decreases in FWHM, and shifts to higher energy with increasing oxidation state (progressing down Fig. 3a), whereas the modulations at higher energy are sensitive to the local atomic environment of the central As atom. The dotted line overlying the AM XANES spectrum in Figure 3c is the result of a linear least-squares fit in which 78% As^{5+} (as scorodite) and 22% reduced As (as arsenopyrite) were used as components (**c**).

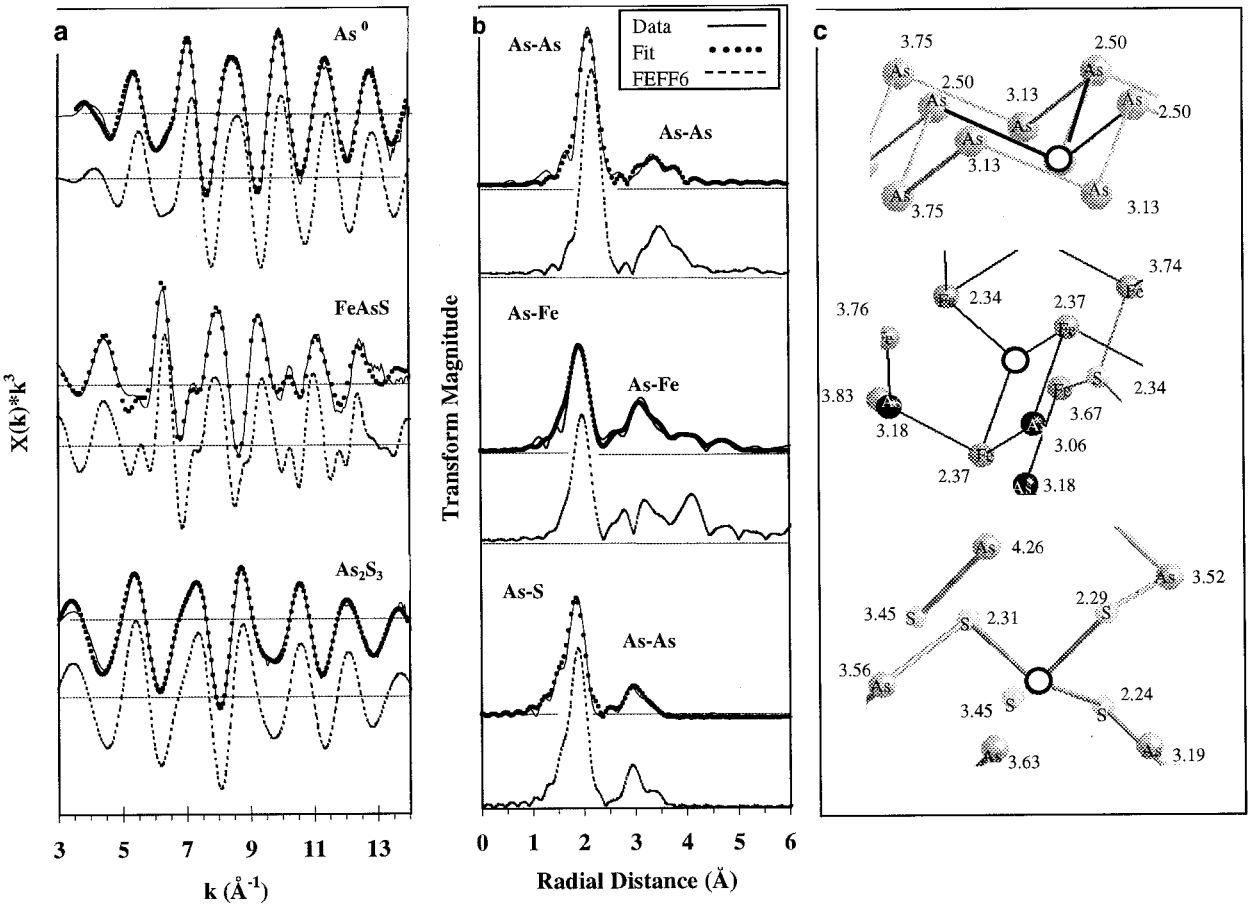

FIGURE 4. (**a**) Normalized, k^3-weighted EXAFS spectra, (**b**) Fourier transforms (FT), and (**c**) schematic illustrations of the As coordination environment (out to ≈4 Å) of reduced As model-compounds. EXAFS spectra and FTs (black lines) are overlain by non-linear, least-squares fits (dots); FEFF6 EXAFS calculations and FTs, including significant multiple scattering paths (where applicable), are plotted as dashed black lines. In (**c**), atomic distances (in Å) from a central As atom (hollow sphere) are given, and nearest-neighbor distances are indicated in boldface type. See Table 3 for a summary of fit parameters.

absorption that occurs over a 10 eV interval beginning at ≈11 865 eV for As^0 and at ≈11 870 eV for As^{5+} compounds. The absorption edge increases in height, decreases in FWHM, and shifts to higher energy with increasing As oxidation state (Fig. 3a).

Comparison of the inflection point of RM, AM, and SM XANES spectra with those of model compounds indicates that these samples contain primarily As^{5+} (Fig. 3b). Sample AM has an additional feature at 11 867 eV, indicating the presence of a reduced-valent As species. Its spectrum is best fit by a combination of ≈80% $FeAsO_4 \cdot 2H_2O$ and ≈20% FeAsS (Fig. 3c). Although EMPA analyses identified pyrite and arsenopyrite in the sample, As^0 could be substituted for FeAsS in the XANES fit without a significant reduction in fit quality, because the nominal oxidation state of As in both compounds is zero. In addition, only the absorption edge of the reduced As component is discernable in the XANES spectrum of the AM sample, whereas XANES structure above the edge is dominated by the As^{5+} component.

EXAFS analysis

Elemental arsenic, arsenopyrite, and orpiment. Figures 4a and 4b display unsmoothed EXAFS spectra, fit results, FEFF6 calculations of EXAFS spectra, and FTs of the reduced model compounds examined in this study. Sb is a significant chemical impurity in our sample of native As, both as a substutional impurity and as a separate phase (SbAs). Thus excess Sb could have several effects on the EXAFS data, including destructive interference of As-As and As-Sb scattering, increased static disorder caused by strain in the As^0 lattice (Fig. 4c, top) arising from substitution of the larger Sb atom, and both effects arising from As present in stibnite (SbAs). We consider these potential effects to be negligible because FEFF6-generated EXAFS spectra of Sb substituted in the first shell of native As (under assumed strain-free conditions) were not noticeably different from FEFF6-generated spectra assuming pure native As. Furthermore, a structural model containing no Sb was used for the final

TABLE 3. Least-squares fits to raw, k³-weighted EXAFS spectra of model compounds

	XRD/FEFF			Least-squares fit					
Sample	*N*	*R* (Å)	*S* (Å)	*N*	*R* (Å)	σ^2 (Å²)	ΔE_0 (eV)	*P* (%)	*F*
As^0									
As-As	3	2.50	0	3*	2.50(3)	0.005(1)	−16(2)	87	85
As-As	3	3.13	0	3*	3.11(5)	0.021(6)		2	
As-As	6	3.75	0	6*	3.74(2)	0.144(2)		8	
As-As	6	4.12	0	6*	4.10(5)	0.022(7)		2	
As-As	3	4.52	0	3*	4.50(1)	0.020(2)		1	
FeAsS									
As-Fe	3	2.36	0.02	3*	2.36(1)	0.008(1)	−10(2)	46	95
As-S	1	2.34	0	—	—	—		—	
As-As	1	3.06	0	1*	3.08(2)	0.005(1)		10	
As-As	2	3.18	0	—	—	—		—	
As-S	3	3.30	0.02	—	—	—		—	
As-As	2	3.32	0	2*	3.35(2)	0.008(3)		22	
As-Fe	4	3.75	0.21	4*	3.76(2)	0.012(3)		10	
As-As	2	4.12	0.10	—	—	—		—	
As-Fe	2	4.21	0.01	—	—	—		—	
As-Fe	2	4.87	0.77	2	4.29(3)	0.010(3)		5	
As-As	2	5.15	0	2*	5.13(3)	0.009(3)		6	
As_2S_3									
As-S	3	2.28	0.03	3*	2.28(1)	0.004(1)	−12(2)	78	44
As-As	1	3.19	—	1*	3.19(1)	0.007(1)		12	
As-S	3	3.45	0.16	—	—	—		—	
As-As	3	3.57	0.06	3*	3.54(1)	0.012(1)		10	
$NaAsO_2 \cdot 4H_2O$									
As-O	3	1.78	0.70	3*	1.78(1)	0.008(1)	−3(2)	72	25
As-As	2	3.23	—	2*	3.27(2)	0.01(1)		28	
As-Na	2	4.65	—	—	—	—		—	
$Na_2HAsO_4 \cdot 7H_2O$									
As-O	4	1.68	0.03	4.9(4)	1.68(1)	0.002(1)	−7(2)	100	136
As-MS	12	4.17	0.02	—	—	—		—	
As-Na	2	4.79	—	—	—	—		—	
As-As	1	6.01	—	—	—	—		—	
$FeAsO_4 \cdot 2H_2O$									
As-O	4	1.68	0.01	6.4(5)	1.68(1)	0.003(1)	−6(2)	60	136
As-MS	14	3.05	—	—	—	—		—	
As-Fe	4	3.35	0.02	4*	3.36(1)	0.004(1)		26	
As-MS	8	3.50	—	—	—	—		—	
As-As	1	4.21	—	1*	4.20(6)	0.006(2)		4	
As-MS	4	4.35	0.01	—	—	—		—	
As-As	2	4.91	—	2*	4.93(4)	0.006(4)		5	
As-As	2	5.41	—	2*	5.44(5)	0.006(3)		5	

Note: Coordination number (*N*), interatomic distance (*R*), and standard deviation of atomic positions (*s*) from structure refinement (see Table 1 for references). Significant multiple scattering paths (As-MS) from FEFF6 calculations (see text). *N, R,* Debye-Waller disorder parameter (σ^2), and threshold energy difference (ΔE_0), obtained from fitting raw data with theoretical phase and amplitude functions (see text). *P* is the contribution of each shell to the total fit, and *F* (goodness of fit) = $\Sigma[\chi(k)^2_{exptal} - \chi(k)^2_{fit}]$. Values for the 95% confidence interval are given in parentheses.

* Assumed value fits.

least-squares fit and FEFF6 calculation, yet these spectra match the experimental spectrum quite well (Figs. 4a and 4b, top).

Arsenopyrite (FeAsS) has a less symmetrical crystal structure than native As (Fig. 4c, top and middle), making it more difficult to group atoms into distinct atomic shells around a central As. This fact is clear from the FT, in which multiple overlapping shells are observed (Fig. 4b, middle). We used only six atomic shells in the least-squares fit, yet achieved a good simulation of the measured spectrum [Fig. 4a (middle) and Table 3]. Unmatched features in the arsenopyrite EXAFS spectrum (Fig. 4a, middle) were not matched by adding a S atom at 2.34 Å or two As atoms at 3.18 Å and constraining their values to those in the reported arsenopyrite structure (Fuess et al. 1987). In contrast to the least-squares fit, all Fe, S, and As atoms within a radial distance of 5.8 Å from the central As were included in the final FEFF6 calculation, which is composed of 22 single-scattering paths and nine high amplitude (>20%) three- and four-legged multiple-scattering paths.

Our fit to the measured EXAFS spectrum of orpiment (Table 3, Fig. 4a, bottom) is in good agreement with the results of a recent EXAFS analysis of this mineral by Helz et al. (1995). We did not include a sulfur shell at 3.45 Å in our final least-squares fit as did Helz et al. because its contribution to the total fit was ≤1%, and therefore negligible. Our final FEFF6-generated EXAFS spectrum, consisting of nine single-scattering paths for As and S atoms out to only 4 Å, provides a good fit to the measured spectrum.

Sodium arsenite, sodium arsenate, and scorodite. The major features in the EXAFS spectrum of $NaAsO_2 \cdot 4H_2O$ were matched well by a model with three first-neighbor O atoms (As-O = 1.78 Å) and two second-neighbor As atoms [As-As = 3.23 Å; Figs. 5a and 5b

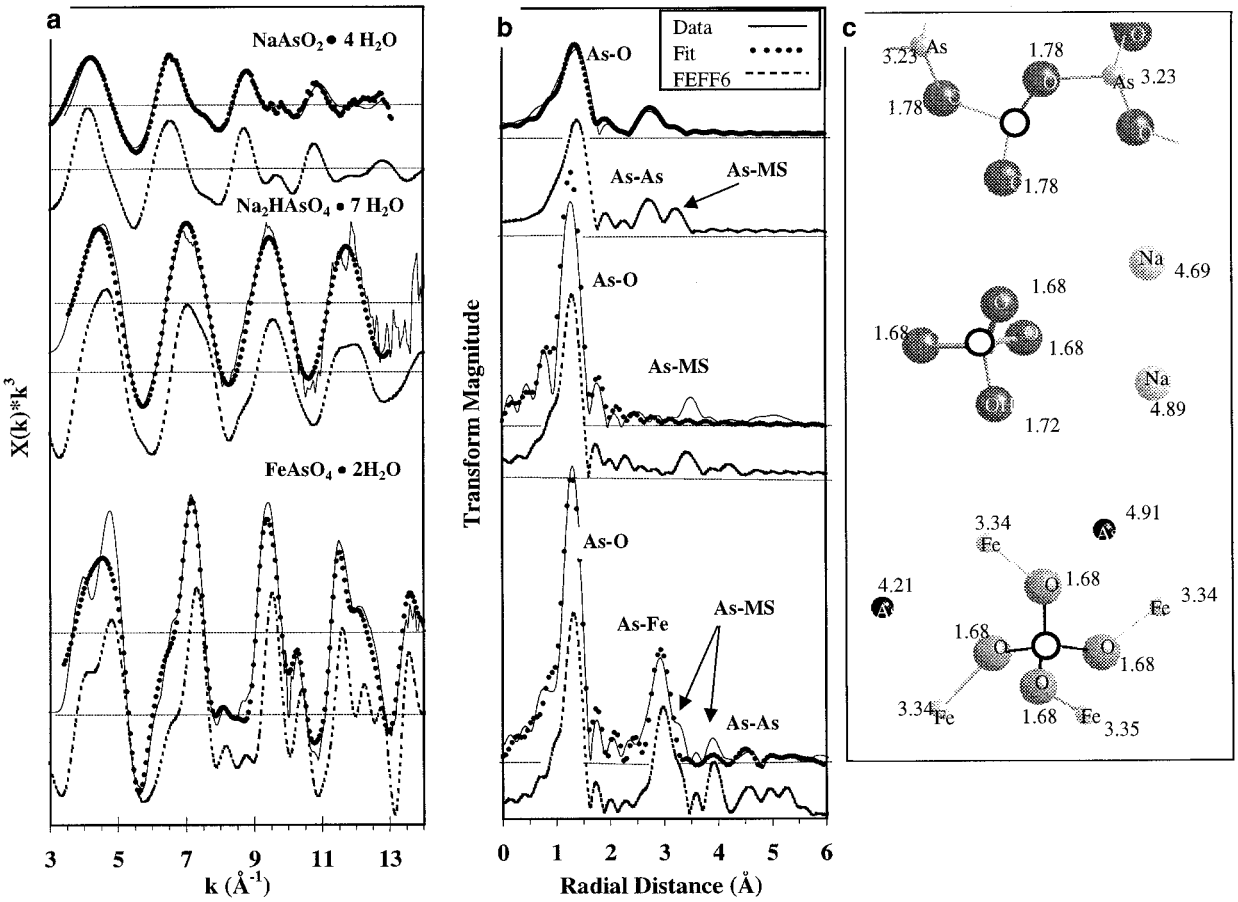

FIGURE 5.(**a**) Normalized, k^3-weighted EXAFS spectra, (**b**) Fourier transforms (FT), and (**c**) schematic illustration of the coordination environment (out to ≈5 Å) of As^{3+} and As^{5+} model compounds. Labeling conventions are the same as Figure 4. Coordinating O atoms in (**c**) have been removed for clarity, except for those in the first shell around As. See Table 3 for a summary of fit parameters.

(top), Table 3]. FEFF6 simulations of this model compound included four single-scattering paths responsible for 90% of the scattering amplitude and several low amplitude multiple-scattering path groups (between 5 and 10% of the maximum amplitude path), which have only a minor influence on the simulated EXAFS spectrum.

$Na_2HAsO_4 \cdot 7H_2O$ contains $AsO_3(OH)$ tetrahedral units (Fig. 5c, middle). The first peak in the FT of the EXAFS spectrum of this compound (Fig. 5b, middle) represents the nearest O and OH neighbors, but the second FT peak at 4.17 Å does not correspond to the positions of second-neighbor Na or As atoms in the known structure (which are located at 4.79 and 6.01 Å, respectively), suggesting that it may arise from multiple-scattering. Our FEFF6 calculations suggest that 12 multiple-scattering paths between the central As and the first- and second-shell O atoms/hydroxyls (with amplitudes ranging from 10–20% of the maximum amplitude path) generate the observed FT feature at ≈3.5 Å (4.17 Å when corrected for phase shift).

Despite the presence of a small amount of carminite in the mineral specimen, the EXAFS spectrum of scorodite (Fig. 5a, bottom) is fit adequately using atomic positions derived from the structure refinement of scorodite (Hawthorne 1976). The final FEFF6 calculation contains 33 paths, ten of which are three-legged, non-linear multiple-scattering paths. The multiple-scattering paths fall into three groups: (1) paths between the first-shell O atoms and the central As atom at 3.04–3.09 Å (FT feature at ≈ 2.6 Å), (2) As-O-Fe paths at 3.4–3.6 Å (FT feature at ≈ 3.0 Å), and (3) paths between the central As, first-shell O atoms, and O atoms coordinating nearby Fe atoms, which give rise to the FT feature at 4.3–4.4 Å [FT features in Fig. 5b (bottom) at ≈3.9 Å]. These multiple scattering paths are collectively responsible for the beat pattern in the first oscillation (≈3.9 $Å^{-1}$), because this feature is not matched by the least-squares fit, which included only single-scattering paths from atoms out to ≈ 6 Å (Fig. 5a, bottom).

Mine tailings. EXAFS analysis of complex, heterogeneous materials such as mine waste is complicated by several factors, including the presence of overlapping

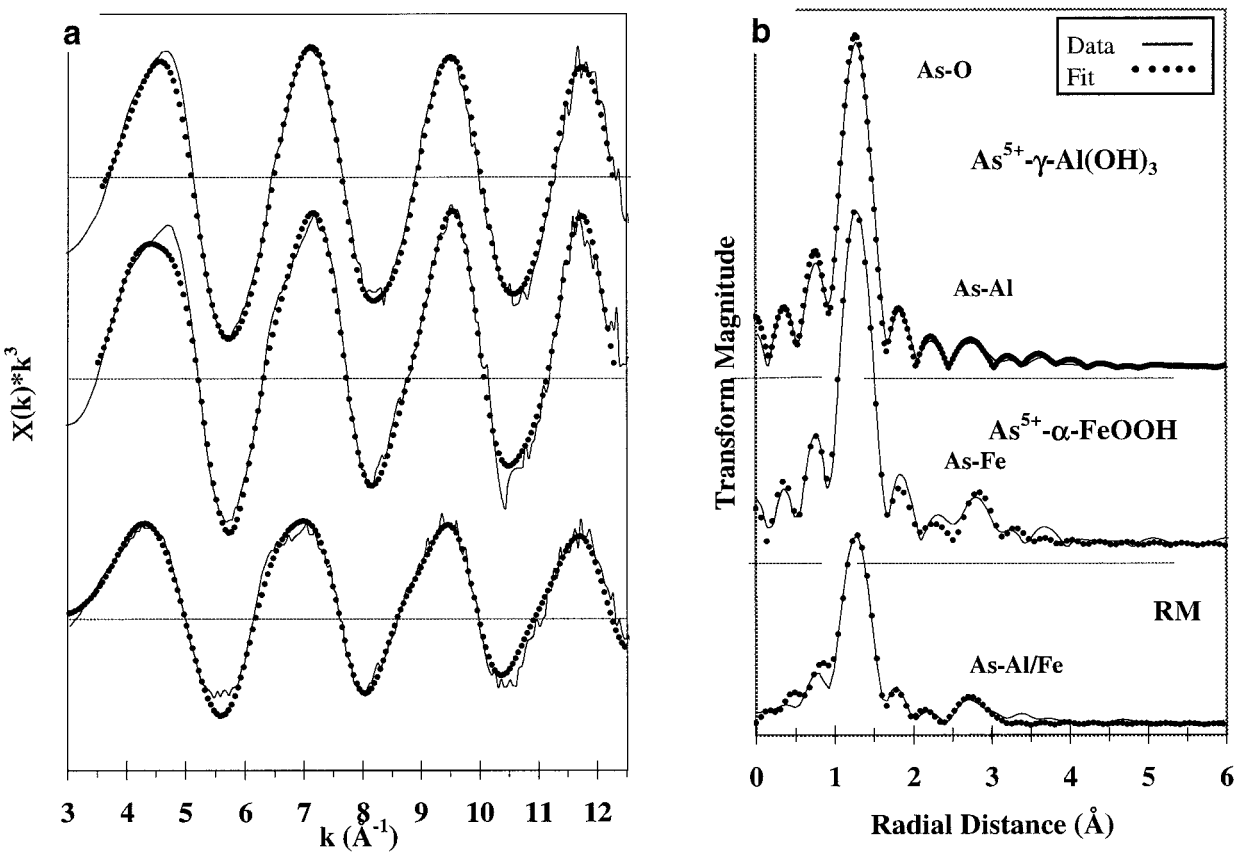

FIGURE 6. (**a**) Non-linear, least-squares fits (dotted lines) to normalized, k^3-weighted EXAFS spectra and (**b**) Fourier transforms (FT) of As^{5+} adsorbed to gibbsite (γ-$Al(OH)_3$), As^{5+} adsorbed to goethite (α-FeOOH), and As^{5+} in the Ruth Mine (RM) sample (solid black lines). The fit to the RM EXAFS data suggests the predominance of two distinct As^{5+} complexes, which together form the second-shell peak (at ≈2.8 Å in Fig. 6b; the As-Fe phase-corrected distance is 3.25 Å). See Table 4 for a summary of fit parameters.

peaks, multi-atom shells, increased disorder due to the presence of poorly crystalline phases, and decreased data quality due to background fluorescence from Fe, which is usually concentrated relative to the element of interest. We thus concentrated on determining the identity of the dominant species of As present in each mine waste. Specifically, we wanted to differentiate between As present as: (1) an adsorbed species, (2) a coprecipitate (used here to denote the incorporation of free As into a mineral structure during its formation or subsequent growth), or (3) a discrete As-bearing phase. As discussed later, the geochemical controls on As release to the environment should be different for each of these modes. The ability to discriminate between multiple chemical species of an element using EXAFS analysis depends on the relative disorder of the species and their relative abundance. A general rule is that chemical species containing approximately 10% of the total As in the sample are normally discernable using EXAFS.

Ruth mine. XRD results indicate quartz, illite, and calcite, whereas iron oxyhydroxide coatings on quartz and calcite grains were detected by EMPA. No crystalline arsenate phases were detected using these methods. Thus the most likely As^{5+} species in sample RM are arsenate sorption complexes or coprecipitates on quartz, illite, calcite, or iron oxyhydroxides. The EXAFS spectrum of sample RM is similar to those of the As^{5+}-α-FeOOH and As^{5+}-γ-$Al(OH)_3$ sorption samples (Fig. 6a), but it is distinctly different from the EXAFS spectrum of scorodite (Fig. 5a, bottom), suggesting similar coordination environments of As^{5+} in the mine waste and sorption samples. In fitting EXAFS data of RM, we considered contributions from Al, As, Ca, Fe, Pb, and Zn, atomic neighbors, and were able to eliminate Pb and Zn. Next we fit the Fourier-filtered, second shell of the RM EXAFS, trying all possible elemental permutations of Al, Ca, Fe, and As neighbors in this shell. A mixed second coordination shell of Al (As-Al = 3.19 Å) and Fe (As-Fe = 3.25 Å) gave the best fit to the raw data (Fig. 7a, middle). The As-Al distance is similar to the As-Al distance of 3.16 Å determined for the As^{5+}-γ-$Al(OH)_3$ sorption sample [Fig. 7a (top), Table 4], but the second-shell As-Fe distance is somewhat shorter than the As-Fe distance determined for the dominant sorption complex in the As^{5+}-α-FeOOH sample (As-Fe = 3.30 Å, Table 3). These second-shell distances appear to be well constrained based on the

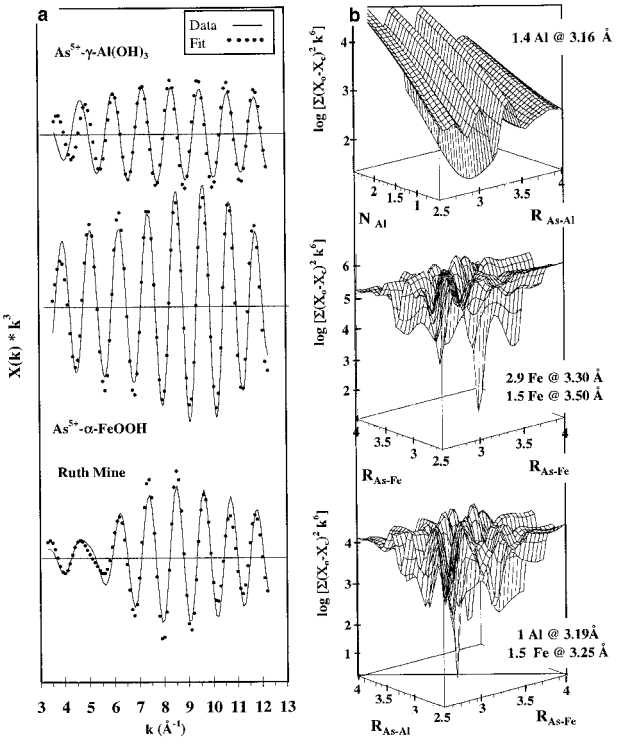

FIGURE 7. (**a**) Second-shell, Fourier-filtered EXAFS spectra (black lines) and least-squares fits (dotted lines) of As^{5+} adsorbed to gibbsite (γ-$Al(OH)_3$), As^{5+} adsorbed to goethite (α-FeOOH) and As^{5+} in the RM mine-waste sample. The associated 3-D search profiles (**b**), allow visual examination of the logarithm of the fit-error space (*z* axis) with the simultaneous variance of two fit parameters over a specified region (plotted on the *x* and *y* axes). Sharp, deep minima in fit error as seen in the search profiles of the As^{5+}-α-FeOOH sorption sample (middle) and the RM mine-waste (bottom) indicate a good fit. The broad, but deep minimum obtained in the fit to the EXAFS spectrum of As^{5+} sorbed to γ-$Al(OH)_3$ (top) is a result of the larger error associated with the coordination number N ($\pm$1 atom) relative to the small error in radial distance R ($\approx$0.02 Å).

TABLE 4. Results of least-squares fits to raw, k^3-weighted EXAFS spectra of sorption and mine waste samples

	Least-squares fit					
Sample	*N*	*R* (Å)	σ^2 (Å^2)	ΔE_0 (eV)	*P* (%)	*F*
As^{5+}-goethite						
As-O	5.1(3)	1.69(3)	0.001(03)	−4(2)	78	76
As-Fe	2.9(9)	3.30(3)	0.007*		15	
As-Fe	1.5(9)	3.50(3)	0.007*		7	
As^{5+}-gibbsite						
As-O	4.9(3)	1.69(3)	0.002(03)	−4(2)	96	61
As-Al	1.4(9)	3.16(3)	0.007*		4	
Ruth Mine						
As-O	3.5(3)	1.69(3)	0.001(03)	−5*	84	41
As-Al	1.0(3)	3.19(3)	0.007*		9	
As-Fe	1.5(6)	3.25(3)	0.007*		7	
Argonaut Mine						
As-O	6(1)	1.73(3)	0.004(03)	6(4)	45	688
As-Fe	2.6(9)	2.41(3)	0.007*		21	
As-Fe	3(2)	3.37(3)	0.007*		13	
As-Fe	3(2)	3.65(4)	0.007*		10	
As-As	4(2)	4.22(3)	0.007*		11	
Spenceville Mine						
As-O	5.6(6)	1.69(2)	0.001(06)	−4(2)	79	317
As-Fe	4(2)	3.25(2)	0.007*		12	
As-Fe	2(1)	3.47(3)	0.007*		12	
As-Ca	4(2)	4.16(4)	0.007*		9	

Note: N, R, Debye-Waller disorder parameter (σ^2), and threshold energy difference (ΔE_0), obtained from fitting raw data with theoretical phase and amplitude functions from FEFF6.01 (see text). *P* is the contribution of each shell to the total fit, and *F* (goodness of fit) = $\Sigma[\chi(k)^2_{exptal} - \chi(k)^2_{fit}]$. Values for the 95% confidence interval are given in parentheses.

* Assumed value fits.

depth and sharpness of the fit error minimum obtained for this parameter (Fig. 7b). As expected, second-shell coordination numbers obtained from these fits are not as well constrained. A striking example of this is shown in the search profile of the fit to the As^{5+}-γ-$Al(OH)_3$ sorption sample (Fig. 7b, top), in which the variation of the fit error as a function of coordination number (N_{Al}) has no well-defined minimum, but the variation of fit error as a function of As-Al distance ($R_{As\text{-}Al}$) clearly converged to a single value. The second-shell As-Al and As-Fe distances that best fit the data can be used to constrain the types of linkages between AsO_4 tetrahedra and the solids present in sample RM. The models in Figure 8 show that As-Al and As-Fe distances vary from as long as 3.6 Å for a monodentate linkage between AsO_4 and an $Al(O,OH)_6$ or $Fe(OH)_6$ octahedron (as might occur on the surfaces of illite grains or a ferrihydrite surface coating on quartz or calcite, respectively) to as short as 2.6 Å for the unlikely possibility of a bidentate linkage between an AsO_4 and SiO_4 tetrahedron, as might occur on the surface of illite or quartz. The observed As-Al and As-Fe distances for sample RM are most consistent with a bidentate linkage between an AsO_4 tetrahedron and two edge-shared $Al(O,OH)_6$ or two edge-shared $Fe(OH)_6$ octahedra (Figs. 8a and 8b, respectively). AsO_4 tetrahedra could possibly be bonded to SiO_4 tetrahedra on illite or quartz surfaces in a monodentate fashion (Fig. 8c), but the ensuing As-Si bond distance is too short to match the As-Al distance and this type of linkage would violate Pauling's second rule (see Bargar et al. 1997). Si could be present because Si cannot be distinguished from Al in the second coordination shell around As by EXAFS spectroscopy (due to their similar backscattering amplitude and phase-shift values).

Waychunas et al. (1993) obtained a second-shell As-Fe distance of 3.25 Å for As^{5+} reacted (adsorbed or coprecipitated) with ferrihydrite, which is a better match to the As-Fe distance obtained from fits to the RM EXAFS data (As-Fe = 3.25 Å) than the As-Fe distance we and others observed for As^{5+} sorption on α-FeOOH (As-Fe = 3.30 Å; Waychunas et al. 1993). Furthermore, we find no XRD evidence for the presence of α-FeOOH in sample RM. Because the second-shell As-Fe distance is identical for As^{5+} sorbed to or coprecipitated with ferrihydrite, sorption vs. precipitation cannot be distinguished. However, the difficulty of liberating As^{5+} from the solid phases in sample RM by sequential extraction methods

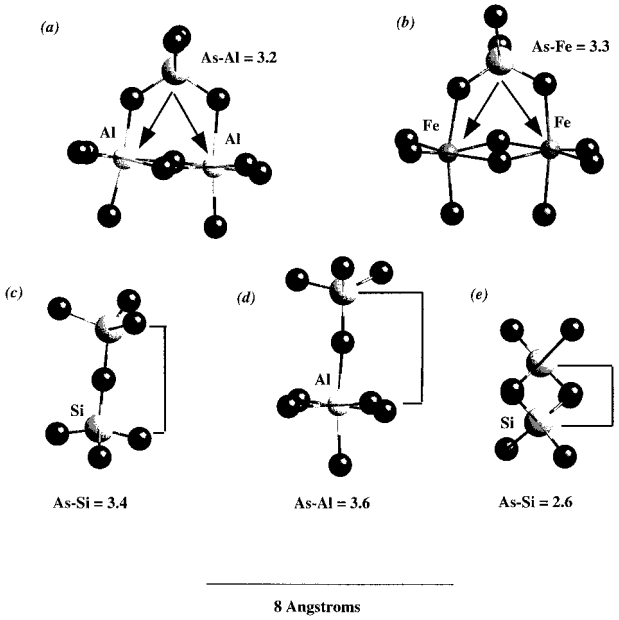

FIGURE 8. Schematic representations of (**a**) an $As^{5+}O_4$ tetrahedron bonded to two adjacent O atoms of edge-shared AlO_6 octahedra (representative of a reactive site on gibbsite or an aluminosilicate mineral), (**b**) an $As^{5+}O_4$ tetrahedron bonded to two adjacent O atoms of edge-shared $Fe^{3+}O_6$ octahedra (representative of a reactive site on goethite, or an iron oxyhydroxide), (**c**) an $As^{5+}O_4$ tetrahedron bonded to an SiO_4 tetrahedron, (**d**) an $As^{5+}O_4$ tetrahedron bonded to an AlO_6 octahedron, and (**e**) an $As^{5+}O_4$ tetrahedron bonded to two O atoms of an SiO_4 tetrahedron. Geometries (**a**), (**c**), (**d**), and (**e**) are representative of possible sorption sites on clay minerals, although (**e**) is not very likely. Geometry (**d**) is also representative of a possible sorption site on gibbsite. Distances shown are approximate, and represent the maximum distance for that particular geometry.

(Borch et al. 1994a) suggests that most of the As^{5+} in the sample RM is probably bound in a coprecipitate with ferrihydrite rather than an adsorbed complex. The remaining As^{5+} may be adsorbed to aluminosilicate phases such as illite, which are abundant in the sample RM. Substitution of As in calcite or precipitation of a ferric arsenate phase, such as scorodite, as a major As species in sample RM is ruled out based on a comparison of the EXAFS with a FEFF6 model of $As^{5+}O_4$ substituted in the calcite structure (As-Ca = 3.21 Å); unsuccessful attempts to fit Ca in the second shell of the RM FT; and comparison with the experimental EXAFS data for scorodite (As-Fe = 3.34 Å).

Argonaut mine. XRD and EMPA analyses indicate the presence of quartz, illite, calcite, arsenical pyrite, and minor amounts of sphalerite, monazite, rutile, and apatite. The EMPA analyses indicate that sphalerite, rutile, monazite, and apatite are essentially As-free. The AM EXAFS and FT have significantly more structure than those of sample RM, suggesting that an appreciable portion of As is incorporated in crystalline phases (Figs. 9a and 9b). Our XANES analysis suggests that ≈20% of the As in the AM mine wastes is incorporated in arsenical pyrite and arsenopyrite in a reduced (nominally As^0) form. Therefore, reduced As in well-ordered mineral phases accounts for some but not all of the observed EXAFS features in the sample AM. Despite the fact that a ferric arsenate precipitate was not directly observed by EPMA and could not be fit with certainty in the Rietveld calculations (always contributing <1% when included in fits), there are several reasons we hypothesize that such a phase should be present. One is the overwhelming predominance of As^{5+} as observed in the XANES spectrum of the sample AM; the small amount of reduced As present could not possibly account for all the features in the FT of sample AM. Second, if 80% of the total As in this sample (262 ppm) is assumed to be present in scorodite, then the relative quantity of scorodite present would be well below the sensitivity of our Rietveld analyses (≈0.2 wt%). Finally, an amorphous ferric arsenate precipitate (which might appear ordered on the short-range scale of EXAFS analysis) of the type likely to form in weathering environments (Krause and Ettel 1988) could escape XRD and EPMA detection if associated with the surfaces of arsenopyrite or arsenical pyrite grains. In the following discussion, we refer to the structures of scorodite and parasymplesite as models for an unknown ferric arsenate precipitate.

Fits to Fourier filtered and raw EXAFS data of sample AM are plotted in Figures 9a and 9b. The results of the filtered EXAFS fits were used as starting parameters for the raw data fit, which is discussed below. The best fit to the AM EXAFS data resulted in six O atoms at 1.73 Å and 2.6 Fe at 2.41 Å (Table 4). The As-O distance is consistent with fourfold-coordinated As^{5+}, but the first-shell coordination number and Debye-Waller factor (σ^2) are unrealistically high for this sample. Based on well-known correlations between first-shell distances and coordination numbers for many oxides (Shannon 1976), we believe that there are only four O atoms in the first coordination shell, and that the value of six atoms resulted from a significant correlation between the coordination number (N) and the disorder parameter (σ^2) of this shell, as also occurred in our fit to the EXAFS spectrum of scorodite (Table 3). Sixfold-coordinated As^{5+} does occur in As_2O_5 (Greenwood and Earnshaw 1984), but we find no XRD evidence of its presence in sample AM, and furthermore, this mineral is not likely to be found in nature. The AM second-shell As-Fe distance (2.41 Å) is considerably shorter than second-shell As-Fe distances reported for $As^{5+}O_4$-containing compounds (3.25–3.35 Å), suggesting that it may represent the primary shell(s) of the As-bearing sulfides present in the AM mine waste. However, the AM second-shell distance is slightly longer than the first-shell As-Fe distance in arsenopyrite, (2.36 Å, this study) and arsenical pyrite (2.31 Å; Tingle et al. 1996), a fact we cannot conclusively explain, but which may be due to difficulties in fitting the strongly overlapped first- and second-shell features of this sample.

In fitting the third-shell feature in the FT of the AM

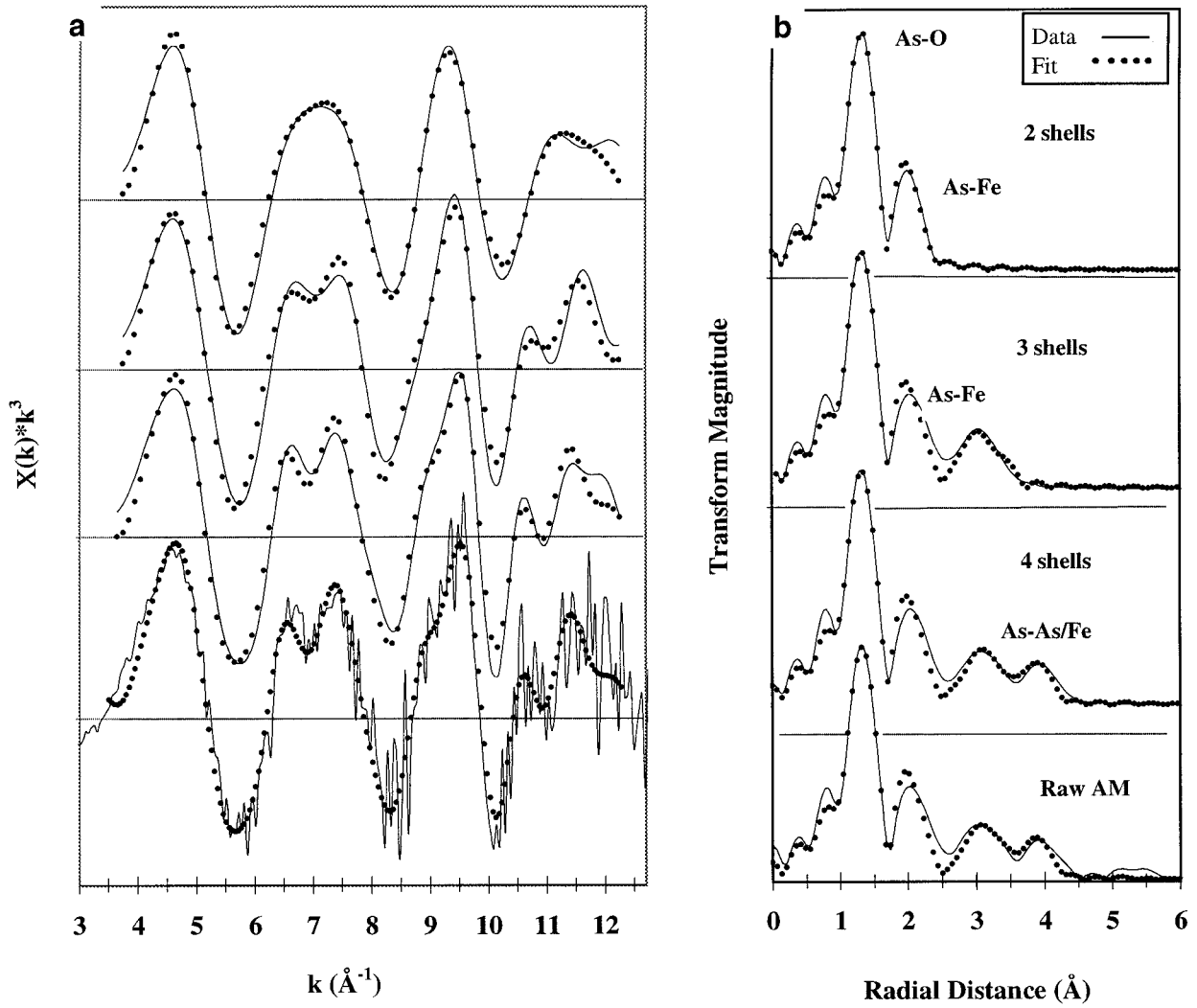

FIGURE 9. (**a**) Least-squares fits (dotted lines) to normalized, k^3-weighted EXAFS spectra (black lines) and (**b**) Fourier transforms (FT) of the Argonaut Mine (AM) sample. The top three spectra in (**a**) are Fourier-filtered EXAFS generated by successively backtransforming the FT of the raw AM EXAFS (**b**, bottom), including an additional FT peak with each backtransform.

sample (Fig. 9b), we tested the possibility of one or two elements in the shell and tried all possible permutations of Fe, Zn, Pb, Ca, and As as third-shell cations. The best fit was given by three Fe at 3.37 Å and three Fe at 3.65 Å (Table 4). The 3.37 Å As-Fe distance is similar to the average second-shell As-Fe distance in scorodite and parasymplesite (3.34 Å for both), but the 3.65 Å As-Fe distance differs from second-shell As-Fe distances in arsenical pyrite (3.48 Å) or arsenopyrite (3.75 Å). However, averaging the second-shell As-Fe distances in arsenical pyrite and arsenopyrite results in an As-Fe distance of 3.62 Å, which is similar to the observed distance of 3.65 Å, and is reasonable given our EPMA and XRD identification of these phases in the sample. In addition, parasymplesite has a single As atom at 3.68 Å that could contribute to this feature. The fourth-shell feature in the AM FT was fit in the same manner, resulting in four As at 4.22 Å (Fig. 9b, bottom). This As-As distance is similar to that found in scorodite, which contains a single As atom at 4.21 Å, whereas arsenopyrite has As and Fe shells at 4.12 and 4.21 Å, respectively. If the As^{5+} in the sample AM is considered to be in a ferric arsenate phase similar to scorodite, it is likely that the As-As shell of scorodite and the mixed As-(As, Fe) shell of arsenopyrite would overlap significantly, resulting in a single peak at ≈4.2 Å, as observed for the sample AM. Based on XANES and EXAFS analysis, ≈80% of the As in sample AM is As^{5+} present in a precipitate, possibly scorodite, parasymplesite, or a poorly crystalline ferric arsenate phase. The remaining As is present in a reduced phase, probably arsenopyrite or arsenical pyrite.

Spenceville mine. XRD and EMPA analyses indicate the presence of hematite, quartz, jarosite, and barite in this sample; scorodite was not observed. The SM EXAFS

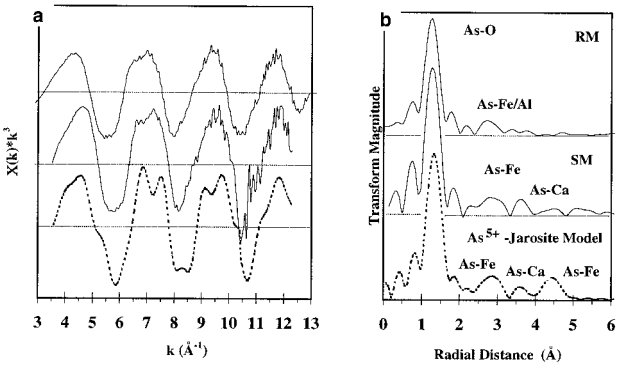

FIGURE 10. (**a**) A comparison of the normalized, k^3-weighted EXAFS spectra, and (**b**) Fourier transforms (FT) of (from top to bottom): the Ruth Mine (RM) sample, the Spenceville Mine (SM) sample, and the FEFF6-generated EXAFS spectrum of As-substituted jarosite.

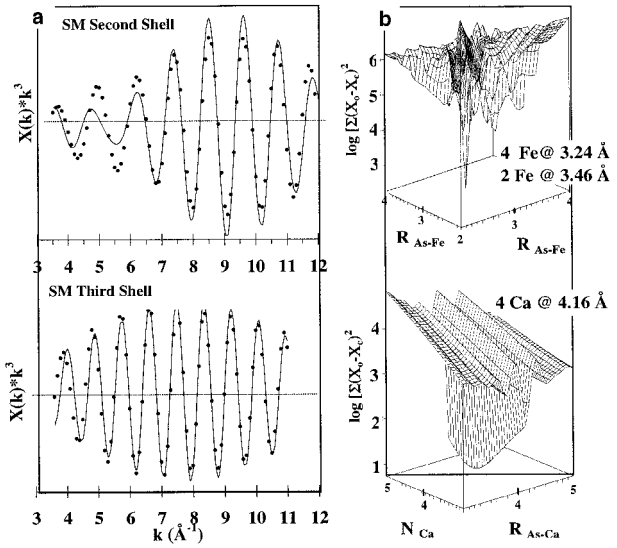

FIGURE 11. (**a**) Second- and third-shell Fourier-filtered EXAFS spectra of the SM mine-waste, overlain by least-squares fits (dotted lines), and (**b**) the associated 3-D search profiles. Labeling conventions as in Figure 7.

appears very similar to the RM EXAFS (except for the first oscillation), and is quite different from a FEFF6 model of arsenate substituted for sulfate in jarosite (Fig 10a). This model does not account for the inherent disorder expected for As^{5+} substituted in jarosite; in particular, the second shell of Fe atoms in jarosite would probably not be as pronounced in experimental EXAFS, just as our FEFF6 model of scorodite overestimates the amplitude of more distant atomic shells (Figs. 5a and 5b). However, comparing the FT's of these samples and FEFF6 models (Fig. 10b), it is clear that the first two shells in the FT's of the SM and RM EXAFS spectra are similar, but the SM FT has a third shell at ≈3.5 Å (4.16 Å, phase-corrected), which is absent in the FT of sample RM. The presence of this shell suggests that either two adsorbed/coprecipitated species of As^{5+} are present in the SM sample, or that As^{5+} is incorporated in a phase of at least local order.

To test these possibilities, we initially fit the second- and third-shell FT features separately (Fig. 11a), then used these results as starting parameters in the raw EXAFS data fit discussed below. The best fit to the second shell of the SM FT contains two different As-Fe correlations, one consisting of four Fe at 3.25 Å, and the second consisting of two Fe at 3.47 Å. The sharp and deep minimum in the least-squares search profile of this shell suggests that the two As-Fe distances are well constrained [Fig. 11b (top)]. The best fit of the third-shell FT feature gives four Ca (or K, which cannot be distinguished from Ca by EXAFS) at 4.16 Å [Fig. 11a (bottom)]. The least-squares search profile of this shell has the appearance of a long, deep trough, suggesting that the As-Ca distance of 4.16 Å is well constrained, but that the coordination number (4 Ca) is not. Barium did not fit well in either shell of the SM FT, suggesting that As substitution in barite is minor.

The As-Fe and As-Ca distances obtained in our fits do not allow unambiguous distinction between adsorbed/coprecipitated As and As substituted in a separate phase. Substitution of an AsO_4 tetrahedron (As-O = 1.69 Å) for a SO_4 tetrahedron (S-O = 1.47 Å) in jarosite results in As-Fe and As-K bond lengths (3.29 Å and 4.16 Å, respectively), which are similar to those obtained by fitting the second and third shells of the SM FT. However, the best-fit SM second-shell As-Fe distances of 3.25 Å could also be obtained by As^{5+} adsorbed or coprecipitated with ferric oxyhydroxides or hematite. Moreover, the As-Fe correlation at 3.47 Å is similar to the As-Fe distance observed for mondodentate linkages in the As^{5+}-α-FeOOH sample (Table 3), which is a reasonable surrogate for As^{5+} sorbed with the same coordination geometry on ferric oxide/hydroxide surfaces. As-Ca distances resulting from FEFF6 models of arsenate substituted in calcite (≈3.2 Å) and gypsum (≈3.1 and ≈3.7 Å) do not match the distance determined from our fit to the third shell of the sample SM, and furthermore, these phases were not found in our Rietveld analyses.

Implications of As speciation in mine-wastes

The observed variability of As speciation (from adsorbed complexes to precipitates) has implications for the mobility, toxicity, and potential bioavailability of As at the three mine sites we have examined. At each of these sites, As^{5+}, which is more toxic and mobile than reduced forms of As predominates As^0. Examination of As^{5+} sorbed on model Fe- and Al-oxyhydroxides suggests that $As^{5+}O_4$ tetrahedra primarily form strong, bidentate complexes on these materials, and by analogy, on the amorphous ferric oxyhydroxide and clay minerals in samples RM and SM. We have also seen evidence of weaker monodentate complexes formed on the surface of goethite (α-FeOOH) in a model adsorption sample; these may also

be present on grains of ferric oxides/hydroxides in the sample SM. Therefore, minimizing the mobility and potential bioavailability of As^{5+} at the RM and SM sites is ultimately dependent upon maintaining environmental conditions at the site which favor As^{5+} retention. Adsorbed As^{5+} is subject to release if the pH or ionic strength of solutions in contact with the acid mine-waste increases dramatically, at which point monodentate complexes should be released more readily than bidentate complexes. The availability of As coprecipitated with ferrihydrite-like material should remain very low in neutral to slightly basic waters.

The Argonaut Mine wastes contain roughly 20% reduced arsenic in sparingly soluble phases such as pyrite and arsenopyrite. If protected from oxidation, these phases retain As in a state of low mobility, toxicity, and bioavailability. As noted earlier, however, *Thiobacillus* species (and other Fe- and S-oxidizing bacteria) can enhance oxidation and dissolution of As-bearing sulfides and release of As unless the dissolved As is sorbed or precipitated in a new form, such as scorodite, or coprecipitated in other minerals (e.g., jarosite). EXAFS indicates that an As^{5+}-bearing precipitate is present in the sample AM (although none was detected by conventional methods) and that a portion of the As^{5+} in sample SM may be substituted in a crystalline phase such as jarosite. The mobility and bioavailability of arsenic in precipitates is generally expected to be lower than for adsorbed arsenic, but these properties depend on the stabilities and solubilities of the As-bearing precipitates. Scorodite (Dove and Rimstidt 1985) and the jarosite minerals (Alpers et al. 1989) are stable only under acidic conditions, thus if the pH increases toward more neutral conditions, arsenic is likely to be released and remobilized. Other, more soluble sulfate minerals, such as aluminum, calcium, and magnesium sulfates, which often form as efflorescences, might also bind As^{5+} in their structures. These are likely to precipitate during the dry summer season, and dissolve during the rainy, winter season, producing a cyclic rise and fall of As concentration in surface and groundwaters.

Acknowledgments

This work was supported by National Science Foundation grant EAR-9406490. A.L.F. acknowledges NSF support in the form of a Graduate Research Fellowship. We thank the staff of the Stanford Synchrotron Radiation Laboratory (SSRL), particularly Ingrid Pickering, Graham George, and Britt Hedman for helpful discussions and technical assistance. SSRL is supported by DOE and NIH. Comments and suggestions from two anonymous reviewers and the associate editor were greatly appreciated. This work is dedicated to the memory of Tracy N. Tingle, our colleague and friend.

References cited

Alpers, C.N., Nordstrom, D.K., and Ball, J.W. (1989) Solubility of jarosite solid solutions precipitated from acid mine waters, Iron Mountain, California, U.S.A. Sciences Gèologiques Bulletin, 42, 281–298.

Anderson, M.A., Ferguson, J.F., and Gavis, J. (1975) Arsenate adsorption on amorphous aluminum hydroxide. Journal of Colloid and Interface Science, 54, 391–399.

Azcue, J.M. and Nriagu, J.O. (1994) Arsenic: Historical Perspectives. In J.O. Nriagu, Ed., Arsenic in the Environment Part 1: Cycling and Characterization, 430 p. Wiley, New York.

Bargar, J.R., Towle, S.N., Brown, G.E., Jr., and Parks, G.A. (1996) Outer-sphere Pb(II) adsorbed at specific surface sites on single crystal α-alumina. Geochimica et Cosmochimica Acta, 60, 3541–3547.

———(1997) XAFS and bond-valence determination of the structures and compositions of surface functional groups and Pb(II) and Co(II) sorption products on single-crystal α-Al_2O_3. Journal of Colloid and Interface Science, 185, 473–492.

Baur, W.H. and Khan, A.A. (1970) On the crystal chemistry of salt hydrates. VI. The crystal structures of disodium hydrogen orthoarsenate heptahydrate and of disodium hydrogen orthophosphate heptahydrate. Acta Crystallographica, B26, 1584–1596.

Bish, D.L. (1993) Studies of clays and clay minerals using x-ray powder diffraction and the Rietveld method. In R.C. Reynolds and J.R. Walker, Eds., Computer Applications to X-ray Powder Diffraction Analysis of Clay Minerals, 171 p. Clay Minerals Society, Boulder, Colorado.

Bish, D.L. and Howard, S.A. (1988) Quantitative phase analysis using the Rietveld method. Journal of Applied Crystallography, 21, 86–91.

Bish, D.L. and Post, J.E. (1993) Quantitative mineralogical analysis using the Rietveld full-pattern fitting method. American Mineralogist, 78, 932–940.

Borch, R.S., Hastings, L.L., and Tingle, T.N. (1994a) A simple gastrointestinal extraction procedure for evaluating the human health risks posed by ingestion of mine waste and contaminated soil. Geological Society of America Abstracts with Programs, 26, 433.

Borch, R.S., Hastings, L.L., Tingle, T.N. and Verosub, K.L. (1994b) Speciation and in vitro gastrointestinal extractability of arsenic in two California gold mine tailings. Eos, 75, 190.

Brown, G.E., Jr., Parks, G.A., and Chisholm-Brause, C.J. (1989) In-situ x-ray absorption spectroscopic studies of ions at oxide-water interfaces. Chimia, 43, 248–256.

Brown, G.E., Jr., Parks, G.A., and O'Day, P.A. (1995) Sorption at mineral-water interfaces: Macroscopic and microscopic perspectives. In D.J. Vaughan and R.A.D. Patrick, Eds., Mineral Surfaces, 370 p. Chapman and Hall, London.

Cebrian, M.E., Albores, A., Garcia-Vargas, G., and Del Razo, L.M. (1994) Chronic arsenic poisoning in humans: The case of Mexico. In J.O. Nriagu, Ed., Arsenic in the Environment Part 1: Cycling and Characterization, p. 93–107. Wiley, New York.

Chen, S.-L., Dzeng, S., and Yang, M.-H. (1994) Arsenic species in groundwaters of the Blackfoot Disease Area, Taiwan. Environmental Science and Technology, 28, 877–881.

Clark, W.B. (1970) Gold districts of California. California Division of Mines and Geology Bulletin, 193, 270.

Cullen, W.R. and Reimer, K.J. (1989) Arsenic speciation in the environment. Chemical Reviews, 89, 713–764.

Dove, P.M. and Rimstidt, J.D. (1985) The solubility and stability of scorodite, $FeasO_4 \cdot 2H_2O$ American Mineralogist, 70, 838–844.

Erlich, H.E. (1995) Geomicrobiology, 719 p. Marcel Dekker, New York.

Fendorf, S.E., Stapleton, M.G., Lamble, G.M., Kelley, M.J., and Sparks, D.L. (1994a) Mechanisms of chromium(III) sorption on silica I: An X-ray absorption fine structure spectroscopic analysis. Environmental Science and Technology, 28, 284–289.

Fendorf, S.E., Lamble, G.M., Sparks, D.L., and Kelley, M.J. (1994b) Investigating solid phases and surface reactions in soils with x-ray absorption fine structure spectroscopy. Soil Science Society of America Journal, 58, 1583–1595.

Frost, R.R. and Griffin, R.A. (1977) Effect of pH on adsorption of arsenic and selenium from landfill leachate by clay minerals. Soil Science Society of America Journal, 41, 53–57.

Fuess, H., Kratz, T., Töpel-Schadt, J., and Miehe, G. (1987) Crystal structure refinement and electron microscopy of arsenopyrite. Zeitschrift für Kristallographie, 179, 335–346.

George, G.N. (1993a) EXAFSPAK. Stanford Synchrotron Radiation Laboratory.

———(1993b) DATFIT. Stanford Synchrotron Radiation Laboratory.

Goldberg, S. and Glaubig, R.A. (1988) Anion sorption on a calcareous,

montmorillonitic soil-arsenic. Soil Science Society of America Journal, 52, 1297–1300.
Greenwald, J. (1995) Arsenic and old mines: As Montanans battle a new gold rush, Californians are dealing with the poisonous legacy of the past. Time, 146, p. 13.
Greenwood, N.N. and Earnshaw, A. (1984) Chemistry of the Elements, 1542 p. Pergamon Press, New York.
Hawthorne, F.C. (1976) The hydrogen positions in scorodite. Acta Crystallographica, B32, 2891–2992.
Helz, G., Tossell, J.A., Charnock, J.M., Pattrick, R.A.D., Vaughan D.J., and Garner, C.D. (1995) Oligomerization in As^{3+} sulfide solutions: Theoretical constraints and spectroscopic evidence. Geochimica et Cosmochimica Acta, 59, 4591–4604.
Korte, N.C. and Fernando, Q. (1991) A review of arsenic (III) in groundwater. Critical Reviews in Environmental Control, 21, 1–39.
Krause, E. and Ettel, V.A. (1988) Solubility and stability of scorodite, $FeAsO_4 \cdot 2H_2O$: New data and further discussion. American Mineralogist, 73, 850–854.
Lytle, F.W. (1989) Experimental x-ray absorption spectroscopy. In H. Winick, Ed., Applications of Synchrotron Radiation, p. 135–233. Gordon and Breach, New York.
Manceau, A. (1995) The mechanism of anion adsorption on iron oxides: Evidence for the binding of arsenate tetrahedra on free $Fe(O,OH)_6$ edges. Geochimica et Cosmochimica Acta, 59, 3647–3653.
Manceau, A., Charlet, L., Boisset, M.C., Didier, B., and Spadini, L. (1992) Sorption and speciation of heavy metals on hydrous Fe and Mn oxides. From microscopic to macroscopic. Applied Clay Science, 7, 201–223.
Manceau, A., Boisset, M.C., Sarret, G., Hazeman, J.L., Mench, M., Cambier, P., and Prost, R. (1996) Direct determination of lead speciation in contaminated soils by EXAFS spectroscopy. Environmental Science and Technology, 30, 1540–1552.
Moore, D.M. and Reynolds, R.C., Jr. (1989) X-ray Diffraction and the Identification and Analysis of Clay Minerals, 332 p. Oxford University Press, Oxford.
Mullen, D.J.E. and Nowacki, W. (1972) Refinement of the crystal structure of realgar, AsS and orpiment, As_2S_3. Zeitschrift für Kristallographie, 136, 48–65.
Myneni, S.C.B., Traina, S.J., Logan, T.J., and Waychunas, G.A. (1997) Oxyanion behavior in alkaline environments: Sorption and desorption of arsenate and ettringite. Environmental Science and Technology, 31, 1761–1768.
O'Day, P.A., Parks, G.A., and Brown, G.E., Jr. (1994a) Molecular structure and binding sites of cobalt (II) surface complexes on kaolinite from x-ray absorption spectroscopy. Clays and Clay Minerals, 42, 337–355.
O'Day, P.A., Rehr, J.J., Zabinski, S.I., and Brown, G.E., Jr. (1994b) Extended x-ray absorption fine structure analysis of disorder and multiple scattering in complex crystalline solids. Journal of the American Chemical Society, 116, 2938–2948.
O'Day, P.A., Chisholm-Brause, C.J., Towle, S.N., Parks, G.A., and Brown, G.E., Jr. (1996) X-ray absorption spectroscopy of Co(II) sorption complexes on quartz (α-SiO_2) and rutile (TiO_2). Geochimica et Cosmochimica Acta, 60, 2515–2532.
Peterson, M.L., Brown, G.E., Jr., Parks, G.A., and Stein, C.L. (1995) Differential sorption and redox of mixed Cr(III/VI) effluent on natural silicate and oxide minerals; EXAFS and XANES results. Geological Society of America Abstracts with Programs, 27, 183.
Pickering, I., Brown, G.E., Jr., and Tokunaga, T.K. (1995) Quantitative speciation of selenium in soils using x-ray absorption spectroscopy. Environmental Science and Technology, 29, 2456–2459.
Pierce, M. and Moore, C.B. (1982) Adsorption of arsenite and arsenate on amorphous iron hydroxide. Water Resources Research, 16, 1247–1253.
Rehr, J.J., Albers, R.C., and Zabinsky, S.I. (1992) High-order multiple-scattering calculations of x-ray absorption fine structure. Physical Review Letters, 69, 3397–3400.
Reynolds, R.A. (1993) The Rietveld Method, 298 p. Oxford University Press, Oxford.
Rimstidt, J.D., Chermak, J.A., and Gagen, P.A. (1994) Rates of reaction of galena, sphalerite, chalcopyrite, and arsenopyrite with Fe^{3+} in acidic solutions. In C.N. Alpers and D.W. Blowes, Eds., Environmental Geochemistry of Sulfide Oxidation, 681 p. American Chemical Society, Washington, D.C.
Sayers, D.E. and Bunker, B.A. (1988) Data analysis. In D.C. Koningsberger and R. Prins, Eds., X-ray Absorption: Principles, Applications, Techniques of EXAFS, SEXAFS, and XANES, 673 p. Wiley, New York.
Schiferl, D. and Barrett, C.S. (1969) The crystal structure of arsenic at 4.2, 78 and 299° K. Journal of Applied Crystallography, 2, 30–36.
Shannon, R.D. (1976) Revised effective ionic radii and systematic studies of interatomic distances in halides and chalcogenides. Acta Crystallographica, A32, 751–767.
Sheldrick, W.S. and Häusler, H.J. (1987) Zur Kenntnis von Natriumarseniten im Dreistoffsystem Na_2O-As_2O_3-H_2O bei 6 °C. Zeitschrift für Anorganische und Allgemeine Chemie, 549, 177–186.
Singh, A. (1995) India grapples with deadly side-effects of irrigation. In Bangkok Post, p. 1.
Spackman, L.K., Hartman, K.D., Harbour, J.D., and Essington, M.E. (1990) Adsorption of oxyanions by spent western oil shale: Arsenate. Environmental Geology and Water Science, 15, 83–91.
Stern, E.A. (1974) Theory of extended x-ray absorption fine structure. Physical Reviews B, 10, 3027–3037.
Tanji, K.K., Ong, C.G.H., Dahlgren, R.A., and Herbel, M.J. (1992) Salt deposits in evaporation ponds: an environmental hazard? California Agriculture, 46, 18–21.
Tessier, A., Campbell, P.G.C., and Bisson, M. (1979) Sequential extraction procedure for the speciation of particulate trace metals. Analytical Chemistry, 51, 844–851.
Tillmanns, E. and Gebert, W. (1973) The crystal structure of tsumcorite, a new mineral from the Tsumeb mine, S.W. Africa. Acta Crystallographica, B29, 2789–2794.
Tingle, T.N., Waychunas, G.A, Bird, D.K., and O'Day, P.A. (1996) X-ray absorption spectoscopy (EXAFS) of arsenic solid solution in pyrite, Clio Mine, Mother Lode Gold District, Tuolumne county. Geological Society of America Abstracts with Programs, 28, 518.
Thompson, H.A., Brown, G.E., Jr., and Parks, G.A. (1997) XAFS spectroscopic study of uranyl coordination in solids and aqueous solution. American Mineralogist, 82, 483–496.
Vogel, N. (1995) Foothills hazard: Homes built on mine tailings, p. 1. San Jose Mercury News.
Waychunas, G.A., Rea, B.A., Fuller, C.C., and Davis, J.A. (1993) Surface chemistry of ferrihydrite: Part 1. EXAFS studies of the geometry of coprecipitated and adsorbed arsenate. Geochimica et Cosmochimica Acta, 57, 2251–2269.
Waychunas, G.A, Davis, J.A., and Fuller, C.C. (1995) Geometry of sorbed arsenate on ferrihydrite and crystalline FeOOH: Re-evaluation of EXAFS results and topological factors in predicting sorbate geometry, and evidence for monodentate complexes. Geochimica et Cosmochimica Acta, 59, 3655–3661.
Yamauchi, H. and Fowler, B.A. (1994) Toxicity and metabolism of inorganic and methylated arsenicals. In J.O. Nriagu, Ed., Arsenic in the Environment Part 1: Cycling and Characterization, 430 p. Wiley, New York.

Manuscript received June 4, 1997
Manuscript accepted November 27, 1997
Paper handled by Hans Keppler